"TEM imaging of dislocation kinks, their motion and pinning". J. Spence, H. Kolar, H. Alexander. J. de. Physique.III, Vol 7, p.2325-2338. 1997. . DMR9526100

TEM imaging of dislocation kinks, their motion and pinning

Short title: TEM kink movies

J.C.H.Spence, H.R. Kolar and H. Alexander*.
Dept. of Physics and SEM, Arizona State University
Tempe, AZ. 85287, U.S.A. Spence@asu.edu
*Universität zu Köln
Abteilung für Metallphysik im II Physikalishen Institut
Zülpicher Str. 77, D 50937, Köln, Germany.

Abstract

HREM lattice images have been obtained using "forbidden" reflections generated by (111) stacking faults in silicon lying normal to the beam at temperatures up to 600^{o}C. Stationary and video images of 30^{o}/90^{o} partial dislocations relaxing toward equilibrium are studied. The lattice images formed from these forbidden reflections show directional fluctuations which are believed to be kinks, since, as expected from mobility measurements, a higher density is observed on 90^{o} partials than on 30^{o} partials, whereas artifacts contribute equally. Video difference images are used to obtain direct estimates of kink velocity. Observations of kink delay at obstacles, thought to be oxygen atoms at the dislocation core, yield unpinning energies and the parameters of the obstacle theory of kink motion. The kink formation energy is obtained from the distribution of kink pair separations in low-dose images. The kink migration rather than formation energy barrier is thus found to control the velocity of unobstructed dislocations in silicon under these experimental conditions.

PACS Numbers 61.70.J, 73.60, 62.20.F

Needs: Suzuki, K. Maedat, N. Takeuchi, S.
Philos. Mag. A, Phys. Condens. Matter Defects Mech. Prop. (UK)
Vol.73, No.2 Feb. 1996 P431-41

1. Introduction

The oldest question in semiconductor dislocation theory remains to be answered - what limits dislocation velocity for given conditions of stress and temperature. Candidates for the rate-limiting process include the double kink formation energy $2F_k$, the migration energy W_m , and kink obstacles, possibly on an atomic scale. In an earlier paper [1], we showed that TEM images formed using certain space-group-forbidden Bragg reflections in silicon maybe used to directly reveal dislocation cores running normal to the electron beam at a resolution of about 0.3 nm. The aim of this work is to address this old question using new lattice images of moving and stationary kinks, obtained by the "forbidden reflection" method [2].The images reveal the position of kinks (with some uncertainty), not their structure. Kink movement was induced by warming in the TEM samples containing quenched-in stacking faults (SF) of non-equilibrium spacing.

It is worth considering first the information which could in principle be obtained from images of kinks, stationary and in motion, at the 0.3 nm resolution level. From recordings of kink velocity at known temperature and stress (as discussed more quantitatively below) an Arhenius plot might yield kink migration activation energies (different for left and right kinks [3]) and, from the pre-factor given by the intercept, the entropy term might also be obtained. Very little is known about this term [4]. These results could be obtained for both partials on dissociated dislocations, comparisons made and the stress dependance of the kink velocity determined. Measurements of kink density at low stress would yield directly the double kink formation energy. But perhaps more importantly, "movies" of kink motion would answer the question "Are kinks colliding" [5], and so provide a direct test of the Hirth-Lothe theory and its two regimes. In addition, the observation of kink delay at obstacles and the measurement of waiting times would yield unpinning energies and provide a test of the obstacle theory of dislocation motion [6]. The proposed correlation between kink nucleation events on different partials could be sought [7]. Finally, the possibility of entirely new phenomena and mechanisms might be observed. All this information could be provided by an imaging method which allows the position of a kink to be localised to within about 0.5 nm, and does not require an image interpretable at the atomic resolution level. Earlier dynamical simulations of HREM images of kinks [8] have shown that obstacles, such as foreign atoms, could not be identified in such images, and many processes (such as kink nucleation at impurites or solitons) would require much higher spatial resolution for structural analysis. The distinction between hetrogeneous and homogeneous kink nucleation could, however, probably be made using our 0.3 nm resolution video images under ideal conditions. In fact our original aim was to make a direct measurement of the nucleation energy barrier (equation 5 below) for comparison with the Seeger-Schiller model, from the measured kink pair distribution function, however this has proven an overly ambitious aim !

Two major experimental difficulties must at once be confronted: the difficulty of distinguishing the effects of atomic-scale surface roughness from kinks in HREM images, which are projections through thin samples, and the effects of electron-beam induced damage or enhancement of glide [9, 10]. Our approaches to these two problems has been as follows. By subtracting successive images which are identical apart from the effects of kink motion we hoped to eliminate the effects of surface roughness. By working below the knock-on threshold for damage, using low-dose techniques and the new Fuji image plates and a CCD camera as detectors, and by turning off the beam during kink motion in certain experiments we planned also to make beam-induced effects negligible. A final difficulty is the accurate control of temperature needed to obtain a kink velocity for given stress which is measurable using video-rate imaging. Thickness variations in the sample mean that only a very limited field of view can be obtained.

Experimental work on kink nucleation and growth in semiconductors is summarized elsewhere [11]; a recent paper proposes several new low energy mechanisms for kink motion [3].

2. "Forbidden" Bragg reflections and their uses.

We commence with a review of the forbidden reflection lattice image method. In 1971, Lynch performed three-dimensional multiple scattering calculations for gold [111] zone-axis electron diffraction patterns, and noted the occurance of additional reflections at the (-422)/3 positions in computed and experimental patterns if the crystal contained $p \neq 3m$ layers of atoms (m an interger) [12]. Figure 1 indicates the location of these reflections. Such reflections are forbidden by the symmetry elements of the space group for a crystal of infinite dimensions. Calculations for similar "termination" reflections in MgO were subsequently reported [13]. TEM dark-field images were first formed with these reflections by D. Cherns in 1974 , who used them to image monatomic surface steps on (111) gold films [14]. Dynamical calculations [15] showed the optimum orientation and thickness to be used. Although there are no termination reflections in the wurtzite structure (because the {-422}/3 reflections are then the fundamental reflections of the three-dimensional hexagonal structure), similar contrast effects have been analysed at SF's in this structure [16]. With the development of ultra-high vacuum transmission electron microscopy, these same termination reflections could be identified in transmission patterns from thin (111) silicon crystals with (7X7) reconstructed surfaces [17] and analysed [18]. These reflections can also occur in f.c.c. and diamond structure materials due to twinning, or to SF's parallel to the surface. They were first observed as additional spots in microdiffraction patterns from stacking faults in 1986, using a field-emission STEM probe narrower than the ribbon of SF separating two partial dislocations [19]. Figure 1 shows such a pattern, obtained recently by H. Kolar using convergent-beam electron diffraction (CBED). Since the edges of the SF ribbon define partial dislocation cores, an image

formed with the inner six of these "termination" or forbidden reflections in the (111) zone provides a lattice image of the SF alone, and its boundary at the dislocation core. The d-spacing for the "forbidden" planes is $d_{422} = h = 0.33$ nm., or one Peierls valley wide. These valleys run along the <011> tunnels in the diamond structure, orthogonal to (42-2)/3. Additional studies based on the use of termination reflections can be found elsewhere [20, 21].

Termination reflections may be understood in several ways. A single (111) double layer of silicon atoms produces a much denser reciprocal lattice (which includes {-422}/3 reflections) than does an infinite crystal. This occurs because atoms in a single double layer are more sparsely packed that those in a [111] projection of three double layers, which overlap in projection, leading to a less dense reciprocal lattice without **g** = (-422)/3 type reflections. Dark field images formed with them show single atomic-height surface steps on thin foils. This can be understood as follows. Firstly we note that, if the [-1,-1,-1] beam direction is taken into the foil, then a (1-11) reflection lies in the first order Laue zone (FOLZ) directly above the $(2,-4,2)/3$ ZOLZ termination reflection shown in figure 1. We can thus consider the $(2,-4,2)/3$ ZOLZ spot to be the tail of the crystal shape-transform (or rocking curve) laid down around the (1-11) HOLZ spot, and extending down into the ZOLZ. Since the (1,-1, 1) reflection is weak in the ZOLZ, kinematic theory can be used to give the intensity of the (1,-1,1) beam as

$$\left|\varphi_g(z)\right|^2 = z^2\sigma^2 V_g^2 \frac{\sin^2(\pi\ z\ s_g)}{(\pi\ z\ s_g)^2} \qquad 1.$$

The period of this function in z (giving rise to thickness fringes) is $L = S_g^{-1}$. The excitation error S_g of the (1-11) FOLZ reflection evaluated in the ZOLZ (i.e. at the $(2,-4,2)/3$ position) is just equal to the height of the FOLZ, or $|g(111)|/3 = (\sqrt{3}/a)/3 = 1/(3d_{111}) = S_{111}$, where a is the silicon conventional cubic cell constant. Thus the period of thickness fringes is $t_o = 3\ d_{111} = 0.94$ nm, and we expect a sinusiodal intensity variation with thickness, with a period of three atomic double-layers. Termination reflections thus give "weak beam" thickness fringes with the period of the lattice in the beam direction.

This approximate treatment assumes that the (2,-4,2)/3 reflection is at the Bragg condition (rather than the [111] zone axis orientation used in these experiments), and it ignores atomic structure within the 0.94 nm spacing along the beam path. Alternatively, we may explicitly evaluate the (2,-4,2)/3 structure factor for silicon. If we choose an unconventional hexagonal unit cell for silicon with the c axis along the cubic [111] direction so that atoms have coordinates such as (1/3,1/3,1/3) etc, then a "forbidden" reflection **g** has hexagonal indicies such as (11.0), and its structure factor becomes

$$V_g = \frac{47.878}{\Omega}\sum_j f_j^e(g)\exp(-2\pi g.r_j) = \frac{47.878}{\Omega}\,2\,f^e(g)\sum_{n=0}^{N}\exp(-4n\pi i/3) \quad 2$$

for a crystal of N double layers, again at the Bragg condition for (2,-4,2)/3 (cubic indicies). Here V_g is in volts, Ω is the cell volume and $f^e(g)$ the electron structure factor. Each term in the final sum is proportional to the scattering from one double layer , and these terms may be represented on an Argand diagram, as shown in figure 2. The imaginary part of V_g has been plotted horizontally and real part vertical. One side of the triangle represents the scattering from a single (111) double layer of atoms in silicon - to analyse the effects of shuffle or glide termination, half the lengths of the sides should be used. The lateral shear of each double layer in the diamond structure introduces a 120^o phase shift, making a closed triangle ABC every three layers with zero resultant scattering. A thin crystal containing 3m double layers above an intrinsic SF and 3n below it has stacking sequence (3m) AB/ABC (3n), as shown. Below the SF the total scattering vector runs from the origin to each of the corners on the upper triangle in turn, and the intensity is never zero. If the scattering amplitude from one double layer is F (with intensity F^2), then the change in intensity due to the addition of a single double layer in an unfaulted crystal is either zero (on adding a B layer to an A layer) or F^2 (for addition of an A or C layer). For a faulted crystal the results depend on the depth of the fault, however all the possible cases may be obtained by starting at one corner of the lower triangle and ending at one on the upper. In particular, for the kink images, we may compare the diffracted intensity produced by a column of crystal within a ribbon of SF with that generated outside it. In the most favorable case, an unfaulted region ABCABCABC produces zero intensity , but a faulted crystal ABCAB/ABCA of the same thickness generates intensity $3F^2$. Multiple scattering calculations [19] confirm these kinematic estimates. Figure 3 shows multislice calculations for the intensity of the (-2-24)/3 reflection as a function of thickness, and we see that the addition of a C layer (shown primed in figures 2 and 3) after the fault changes the intensity by about $4F^2$, in agreement with figure 2. These calculations (unlike figure 2) correctly take account of the excitation errors for the termination reflections, and when this is done we find that the six {-422}/3 reflections are not equivalent - there are two groups of three, reflecting the three-fold (not six-fold) symmetry of a (111) slab consisting of $p \neq 3m$ layers. At the [111] zone axis orientation the forbidden reflection intensity nevertheless still falls to zero every three double layers.

Real crystals have atomically rough surfaces, and these effects must also be considered, in addition to other sources of background in the images, which limit contrast. A full analysis has been given, [19], but the main points are as follows. TEM cross section lattice images of Si/SiO_2 interfaces suggest that the roughness will be one or two double-layers, and no images were recorded if contamination could be seen growing at the edges of our samples. Large atomically flat surface islands produce sharp forbidden reflections unless p =3m. As the island size becomes small

compared with the coherence width of the electron beam these forbidden reflections broaden out into diffuse elastic scattering peaks. For a random distribution of surface vacancies there are no termination reflections. The width of the diffuse peaks increases with the depth of the surface roughness. We can understand this by recalling that the projected potential for a thin "perfect" crystal with atomically rough surfaces is not a periodic function, hence its diffraction pattern contains elastic diffuse scattering. Because we do not see surface islands in forbidden reflection lattice images from unfaulted crystal, we assume that the roughness can be modelled as random vacancies in the surface layer. Depending on the crystal thickness, these vacancies may or may not lie within the atomic column which contains a kink, thereby altering its contrast. The still images of dislocation cores, however, show a much higher density of kinks on the 90^o partial dislocation than on the 30^o partial, suggesting that surface roughness is not the dominant contrast effect. In addition, by digital subtraction of sucessive video frames we can isolate the moving kinks from the stationary surface noise. Figure 3 shows that the average image intensity from by a rough, faulted crystal is higher than that of a rough, unfaulted crystal, and kinks form the boundary between these regions. (The average scattering, rather than the image intensity, from a crystal with a uniform distribution of terminations is represented by a point in the center of each triangle). Nevertheless, in still images this surface roughness contributes a large error to our estimates of kink concentration. (The error is calculated by tracing every reasonable boundary to the SF). The ability to introduce dislocations in-situ into a sample whose surfaces have been cleaned by heating in-situ would improve the quality of our images, but would also superimpose the silicon (7X7) reconstruction onto the images.

3. Dynamic observations and pinning.

Our first experiments consisted of TEM video recording of partials relaxing toward their equilibrium spacing at 600^oC. Our silicon samples were formed by a two stage deformation process, ending with cooling under high stress [22]. This produces stacking faults on (111) of non-equilibrium width d, which relax back to equilibrium if the sample is warmed in the microscope. TEM samples were prepared by chemical etching at room temperature (no hot glues). In equilibrium, the elastic repulsive force between the partials is just balanced by the attractive force resulting from the work needed to create SF, and the SF width is d= 5.8 nm. Otherwise the shear stress σ in the direction of the partial Burgers vector b can be determined if d is known using $\sigma = (\gamma - (A/d)) / b$, where the SF energy $\gamma = 0.058$ J m^{-2} for Si, and $A = 3.36 \times 10^{-10}$ N. Video recordings were obtained during this relaxation on the Akashi 002B TEM using the Gatan heating stage, at 0.25 nm resolution at temperatures of 600^oC (above the kink nucleation temperature). The objective aperture shown in figure 1 was used. The beam remained on during the dislocation motion

and video recording.Figure 4 shows a sketch of the experimental geometry used. In 4(a) the diagonal lines are the [011] "tunnels" , or Peierls valleys,through the diamond lattice, with separation 0.33 nm. Kinks are shown at K and K' where the dislocation throws a loop of line forward into the next [011] low energy valley by nucleating a kink pair. The line advances in direction V if the kinks move apart to the end of the segment, or until they collide with kinks of opposite sign. Figure 4(b) shows a side view. The SF plane generates six <42-2>/3 Bragg beams within the SF ribbon and not elsewhere, and only these are used to form the images. The d-spacing for the planes is d_{422} = h = 0.33 nm., or one Peierls valley wide. These valleys run along the <011> tunnels in the diamond structure, orthogonal to (42-2)/3.

Video rate images of several 60^o dislocation segments dissociated into 30^o and 90^o partials were recorded at 600^oC. Consistent with the earlier finding that 90^o partials are more mobile than 30^o partials [11], motion (on the atomic scale) was confined to the 90^o partial, and, accordingly, later stationary images of quenched samples showed a higher kink density on the 90^o partial than on the 30^o partial. (Mobility depends on which partial is leading or trailing [11]). Figure 5(a) shows the difference between video frames recorded before and after motion of a $90^o/30^o$ dislocation at $600^o \pm 10^o$ C. In principle, such a difference image should show zero intensity everywhere except in the region where SF has been created or elliminated. The high constrast outside this region is due to noise, which has been amplified in the process of increasing the contrast digitally in order to reveal the SF, which is the dark strip. Observations at the edge of the sample showed no growth of contamination. The overall SF is narrowing toward equilibrium by motion of the 90^o partial alone. Cross-correlation between stationary regions was used to align successive video frames, which are inherently noisy. The dark region is a thin strip of SF on the 90^o partial, whose width measured normal to the dislocation line is three Peierls valleys (3 d_{422} =0.99 nm). This strip, suggested by the crossed shading in Figure 4(a), has been eliminated by the passage of several kinks moving parallel to V_k shown. The kinks encounter obstacles at K and K'. Figure 5(b) shows the collapse of a segment of SF whose width is one Peierls valley (0.33nm) wide. A study of individual frames shows that the motion spans several 33ms frames, so that upper and lower limits on the kink transit time can be made with an error of one frame. A typical single-width segment L = 11.7 nm long gave a velocity of 205 ± 111 nm/sec , at 600^oC. The stress $\sigma = 108.5 \pm 7.5$ Mpa, was obtained from the total SF width of 9.95 ± 0.5 nm. From the waiting times $\tau = \nu_D^{-1} \exp(E_u/kT)$ at obstacles such as K and K' in figure 4(a) unpinning energies E_u may also be obtained -the average of two single-width cases gave $E_u = 2.4 \pm 0.04$ eV. Applying the obstacle theory of kink motion [6, 7, 23] we obtain a velocity $v'_k = L \nu_D \exp(-E_u/kT) = 2.4$ nm/sec for the average velocity of kinks encountering many obstacles. A comparison with the instantaneous kink velocity of 205 nm/sec shows that the transit time is short compared with the waiting time, as assumed in obstacle theories. Several experimentally indistinguishable kink mechanisms may be responsible for these

observations - in particular we cannot distinguish single kink unpinning at one end of the segment K from homogeneous double kink nucleation at mid-segment followed by outward propagation to obstacles K, K' at the ends of the segment. Since extended defects are not seen at cores in still images at atomic resolution, the obstacles are most likely to be dragging points which move forward with the line. We now consider the likely origin of the obstacles.

During the 800^{o}C first stage of deformation, dislocations getter the P ($2x10^{13}$ cm^{-3}), O ($<10^{16}$) and C ($<10^{16}$) impurities in our FZ sample. Carbon is known to be ineffective in dislocation pinning [24]. Vacancies and interstitials have much larger values of L, as does P (although strongly pinning) due to its low diffusion rate [25]. We find no evidence (at 0.27 nm resolution) for the O or P complexes previously proposed as pinning centers [26, 27]. We see no evidence of climb-induced pinning. The impurity with highest concentration is oxygen, whose pinning effect has been studied extensively by X-ray topography in samples with controlled impurity concentrations. This work suggests [28], at high temperature, an oxygen pinning center with L ≈ 14.0 nm and an unpinning energy of about 3 eV. Ab-initio electronic structure cluster calculations for a variety of likely structures suggest [29] that a single oxygen atom on the most stretched bond around the anti-phase (soliton) defect can explain this X-ray imaging result. The concentration and unpinning energy (release rate) of this defect are in rough agreement with our observations, however beam induced pinning effects must be considered. Previous work [30, 31, 32] suggests that the beam has two effects a) At energies above the threshold for ballistic knock-on damage (about 140 kV) strong pinning centers are introduced, and b) Enhanced diffusion of kinks (REDG) and impurities by beam-induced electron-hole pair recombination at these defects occurs [33]. The first effect was minimized by conducting a series of experiments in which the beam energy was reduced until, at 130 kV (where all this work was done), the concentration of resolvable beam-induced defects was found to be negligible. (Knock-on damage is easily visible in lattice images at higher voltages). The second effect depends on the intensity and duration of tbe exposure. The spacing of these obstacles is consistent with the "garland" and cusp features seen on 90^{o} partials in previous work, thought to be due to recombination enhanced diffusion of impurities from the thin foil surfaces to dislocations [34], and which are not seen in unirradiated samples. The ability of impurities to create a soliton-antisoliton pair on arrival at a reconstructed core, and for these sites subsequently to nucleate oxide precipitates, has been noted [35]. In summary, we speculate that the 2.4 eV unpinning energy we observe is due to oxygen at anti-phase defects, affected in some way by irradiation. Self interstitials may also be involved.

4. Kink migration energy

By analysing the motion of a partial at a temperature low enough to ensure that no new kinks are created during the motion, the kink migration energy can be determined if the kink density is

known. The velocity of a kink of height h, for a dislocation with Burgers vector b and core period *a* is

$$v_k = \frac{\sigma b h \nu_D a^2}{kT} \exp(-W_m / kT) = \frac{\sigma b h}{2kT} D_p \qquad 3$$

where ν_D is the Debye frequency (1.3×10^{13} sec^{-1} - more strictly the phonon frequency in the direction of motion should be used) , D_p the double kink diffusion coefficient and $W_m = U_m - TS_m$ is the free energy (strictly enthalpy) of kink migration, U_m an enthalpy (experiments are performed at constant pressure). (Similarly $F_k = U_k - TS_k$). Theoreticians compute internal energies U'_m (the sum of elastic and core energies, usually computed at constant volume); experiments measure either W_m or U_m (depending on data analysis). Our U_m values assume [4] $S_k(90^o) = 0.5$ k and $S_m(90^o) = 5$k)

Stationary images were therefore recorded on video and film of a $30^o/90^o$ dislocation under low dose conditions (to avoid the introduction of pinning centers), both before and after annealing at 130^oC (below the kink nucleation temperature) for 15 mins. The electron beam was switched off during the dislocation motion. Figure 6 shows a typical lattice image formed from the inner six "forbidden" reflections in figure 1. The partials have moved apart in the TEM toward their equilibrium separation of 5.8 nm. (Unlike 90/30 dislocations and screws, the $30/90$ contracts during the initial ex-situ deformation due to lattice friction [11]). Image calculations [8] show that the bright diagonal band of regularly spaced dots is a lattice image of the double layer of atoms (spaced 0.33 nm apart) which form the SF plane. (Extrinsic and intrinsic faults produce similar images). Pairs of atoms appear as a single dark spot, bright spots are centered on the six-fold rings of a single double-layer. The borders of this band of regular dots forms the partial dislocation cores, as shown. The white scale lines indicate one Peierls valley, 0.33 nm wide. The average SF width corresponds to a stress on the partials of 275 MPa . We note that the density of kinks is greater on the 90^o partial than on the 30^o partial (see also figure 7). An accurate determination of kink density is complicated by the effects of surface roughness, however the higher density on one partial (seen also in larger fields of view such as figure 7 and in many different cases [19]) suggests that surface effects are not dominant. In addition, monatomic surface islands are not seen outside the SF - these would produce similar (but lower) contrast to the SF. "Kinks" smaller than the critical separation x* = 0.81 nm (defined below) are evidently due to surface roughness. Figure 6 shows how the error in kink density was estimated. These images may be used to estimate W_m from the kink density c and distance Δs the partial dislocation moves (with beam off), using $V_{dis} = 2\,c\,h\,V_k = \Delta s/\Delta t$, where h = 0.33 nm, the kink height. Now $v_k \Delta t = \Delta y$, hence $\Delta s = 2ch\Delta y$, where Δy is the mean distance a kink moves in time Δt . Using $\Delta y / \Delta t = v_k$ in equation 3 yields $W_m = 1.24 \pm 0.07$ eV (U_m =

1.55 eV). (Within our limited field of view, less than the kink mean free path, obstacles are unimportant if present in unirradiated material). Figure 7 shows a still from a low-dose video frame for a different dislocation, in this case an unrelaxed pair of partials more narrowly spaced than their equilibrium separation.

5. Kink nucleation energy

By measuring the distribution of kink-pair separations in these images, the kink formation free energy F_k may be estimated. This could be most easily done under conditions of low stress, when the concentration of kinks is close to thermal equilibrium, and simply related to F_k by a Boltzmann factor. Our annealing experiments were unsuccessful is providing a sufficiently large field of view of fully relaxed partials within the acceptable range of sample thickeness for good imaging. It was therefore necessary to use the high stress theory of dislocation motion to analyse our images. The most successful theory of dislocation motion [36] (but see [5]) considers the nucleation of double kinks (with separation x), their diffusion and drift under an external stress σ by one-dimensional analogy with classical steady-state nucleation theory for particles of size x. Then the distribution of kink separations (constrained to zero kink current) per unit length of line is

$$c_c(x) = \frac{1}{a^2}\exp(-F(x)/kT) \qquad 4$$

with dims L^{-2} . Here the free energy of kink-pair formation in the presence of the large stresses used in our experiments is [37]

$$F(x) = 2F_k - \frac{\mu b^2 h^2}{8\pi x} - \sigma b h x \qquad 5$$

where μ is the shear modulus. The second term represents the attractive kink-kink strain interaction (tending to annihilate by recombination kink pair embryos less then the critical separation x*) while the last term describes the external stress, driving kinks apart. The net double kink nucleation rate is $J = D_p C_o(x^*)/2x'$, and the dislocation velocity $V = 2h(Jv_k)^{1/2}$ if the dislocation segment length is larger than the kink mean free path λ. Then V depends exponentially on $Q = F_k + W_m$. Here $x' = kT/(\sigma bh)$. Other theoretical treatments have assumed that kink velocity is limited by obstacles (such as anti-phase defects, impurities or point defects) [6, 7, 23] . Several theoretical calculations for W_m and F_k have been published [38, 39].

Table 1 shows the distribution of kink pair separations measured from images such as figure 6. The large error was obtained by drawing in all reasonable core boundaries. From the table, values of c(x) (with dims L^{-2} , not L^{-1}) , the unconstrained number of kink pairs with separation between

x and x+dx per unit length of dislocation may be obtained. The critical separation at the saddle point is $x^* = (\mu b h / 8\pi\sigma)^{1/2} = 0.81$ nm. By extrapolation from Table 1 we obtain $c(x^*) = 8.9 \times 10^7$ m^{-2}, which, according to Zeldovich [40] is half the constrained value $c_o(x^*)$. Using eqn. 4 with a =0.384 nm, T = 420^{o}C gives $F(x^*) \approx 1.455$ eV , so that, from eqn. 5, $F_k = 0.5 (F(x^*) + (\mu \sigma b^3 h^3 / 2\pi)^{1/2}) = 0.727 \pm 0.15$ eV ($U_k = 0.74$ eV). This may refer either to a reconstructed kink, or to a kink associated with a soliton dangling bond.

6. Conclusions.

Measurements on the 30^o partial give approximately one-third the kink density as the 90^o. Thus we find $F_k(30) = 0.797 \pm 0.15$ eV. Our value of $W_m = 1.24$ eV may be compared with recent ab-initio LDA calculations, which give 1.8 eV [41] and is consistent with recent ab-initio calculations [42] favoring reconstruction of the 90^o core, which hinders kink motion (by doubling the jump distance) and clears the band-gap of deep states . Our value is consistent with values of 1.0 - 1.2eV measured previously [30, 34]. Our finding that $F_k = 0.727$ eV may be compared with measurements by other methods which fall in the range 0.4 to 1.1 eV [38, 43], and with calculations giving 0.1 eV [41], based on a hydrogen terminated cluster for the smallest kink pair, with elastic interactions dominating. (These authors comment that their method may underestimate F_k). For segments much longer than the kink mean free path we thus obtain $Q = F_k + W_m = 0.727 + 1.24 = 1.97 \pm 0.2$ eV. Since Fk < Wm, we find that, unlike metals, kink mobility rather than formation is the rate-limiting step controlling the motion of free dislocations in silicon. Since we cannot demonstrate the absence of widely spaced or unresolvable obstacles in unirradiated material, this work cannot distinguish the obstacle [6] and secondary Peierls-valley [36] theories of kink motion. In irradiated material, unpinning of kinks at obstacles is directly observed for the first time, yielding the parameters of the obstacle theory.

Acknowledgements

Supported by N.S.F. award DMR9526100. We are grateful to Drs. R. Jones, P. Pirouz and W. Schröter for useful discussions.

References.

[1] H. Alexander, J. Spence, D. Shindo, H. Gottschalk, N.Long, Phil. Mag, A53, (1986) 627
[2] H. Kolar, J. Spence and H. Alexander, Phys. Rev. Letts., In press, (1996) ,
[3] V. V. Bulatov, S. Yip and A. S. Argon, Philos. Mag., A72, (1995) , 453
[4] S. Marklund, Solid State Communications, 54, (1985) , 555
[5] K. Maeda and Y. Yamashita, Phys Stat Sol, (a)138, (1993) , 523
[6] V. Celli, M. Kabler, T. Ninomiya and R. Thomson, Phys. Rev., 131, (1963) , 58
[7] H. J. Moller, Acta Met, 26, (1978) , 963

[8] J. Spence, Proc.39th Ann Mtng. Electr. Micros.Soc.Am. (1981). G. Bailey, Ed. (Claitors, Baton Rouge). (1981) , 120
[9] M.Werner, E.Weber, M. Bartsch, U.Messerschmidt, Phys. Stat. Sol. (a)150, (1995), 337
[10] K. Kusters and H. Alexander, Physica 116B, (1983) , 594
[11] H. Alexander and H. Teichler, Dislocations (VCH, Weinheim, 1991)
[12] D. F. Lynch,Acta Cryst., A27, (1971) , 399
[13] P. Goodman and A. F. Moodie,Acta Cryst., A30, (1974) , 280
[14] D. Cherns, Phil Mag, 30, (1974) , 549
[15] J. Spence, Proc. EMAG 1975. Inst. of Phys. (1975) p. 257
[16] R.Glaisher, M.Kuwabara, J.Spence, M.McKelvy, Inst. Phys. Conf. Ser., 87, (1987) , 349
[17] Y. Tanishiro, K. Takayanagi and K. Yagi,J. Micros., 142, (1986) , 211
[18] J. C. H. Spence, Ultramicrosc., 11, (1983) , 117
[19] H. Alexander, J.Spence, D.Shindo, H.Gottschalk, N.Long, Phil Mag, 53, (1986), 627
[20] S. Iijima,Ultramic, 6, (1981) , 41
[21] A. Ourmazd, G. Anstis and P. Hirsch, Phil Mag., A48, (1983) , 139
[22] K. Wessel and H. Alexander, Phil. Mag., 35, (1977) , 1523
[23] V. Rybin and A. Orlov, Sov. Phys. Solid State, 11, (1970) , 2635
[24] K. Sumino, J. de Phys., 44, (1983) , C4
[25] K. Sumino and M. Imai, Phil Mag, A47, (1983) , 753
[26] K. Sumino,Inst. Phys. Conf. Ser., 104, (1989) , 245
[27] K. Sumino,Mat. Res. Soc. Symp. Proc., 14, (1983) , 307
[28] M. Sato and K. Sumino,University of Tokyo Press, (1985) , p.391
[29] A. Umerski and R. Jones, Phil Mag, A67, (1993) , 905
[30] P. B. Hirsch, A. Ourmazd and P. Pirouz, Inst. Phys. Conf. Ser., 60, (1981) , 29
[31] A. Louchet, Phil Mag, 43, (1981) , 1289
[32] H. Gottschalk,Electron Microscopy 1982, Vol 2, (1982) , 527
[33] N. Maeda and S. Takeuchi, Inst. Phys. Conf Ser., 104, (1989) , 303
[34] H. Gottschalk, H. Alexander and V. Dietz, Inst. Phys. Conf Ser 87, 87, (1987) , 339
[35] M. Heggie, R. Jones and A. Umerski, Phys. Stat. Sol., (a)138, (1993) , 383
[36] J. P. Hirth and J. Lothe, Theory of dislocations (Wiley,New York,1982)
[37] A. Seeger and P. Schiller, Acta Met, 10, (1962) , 348
[38] H.Gottschalk, N. Sauerland,S.Specht,H.Alexander, Phys. Stat. Sol, (a)138, (1993) , 547
[39] Y. Huang, J. Spence and O. Sankey, Phys. Rev. Letts., 74, (1995) , 3392
[40] J. B. Zeldovich, Acta Physiochem USSR, 18, (1943) , 1
[41] S. Oberg, P. Sitch, R. Jones and M. Heggie, Phys. Rev., B51, (1995) , 13138

[42] J. Bigger, D. McInnes, A. Sutton, M. Payne, I. Stich, R. King-Smith, D. Bird and L. Clarke, Phys. Rev. Letts., 69, (1992) , 2224

[43] R. Hull and J. C. Bean, Phys. Stat. Sol., A138, (1993) , 533

Table 1

N	m	x (nm)
3	4	1.5
2	5	1.9
2	6	2.3

The measured number of kink pairs N with separations x = ma (m integer, a=0.384 nm core period) for a 90^{o} partial dislocation in silicon.

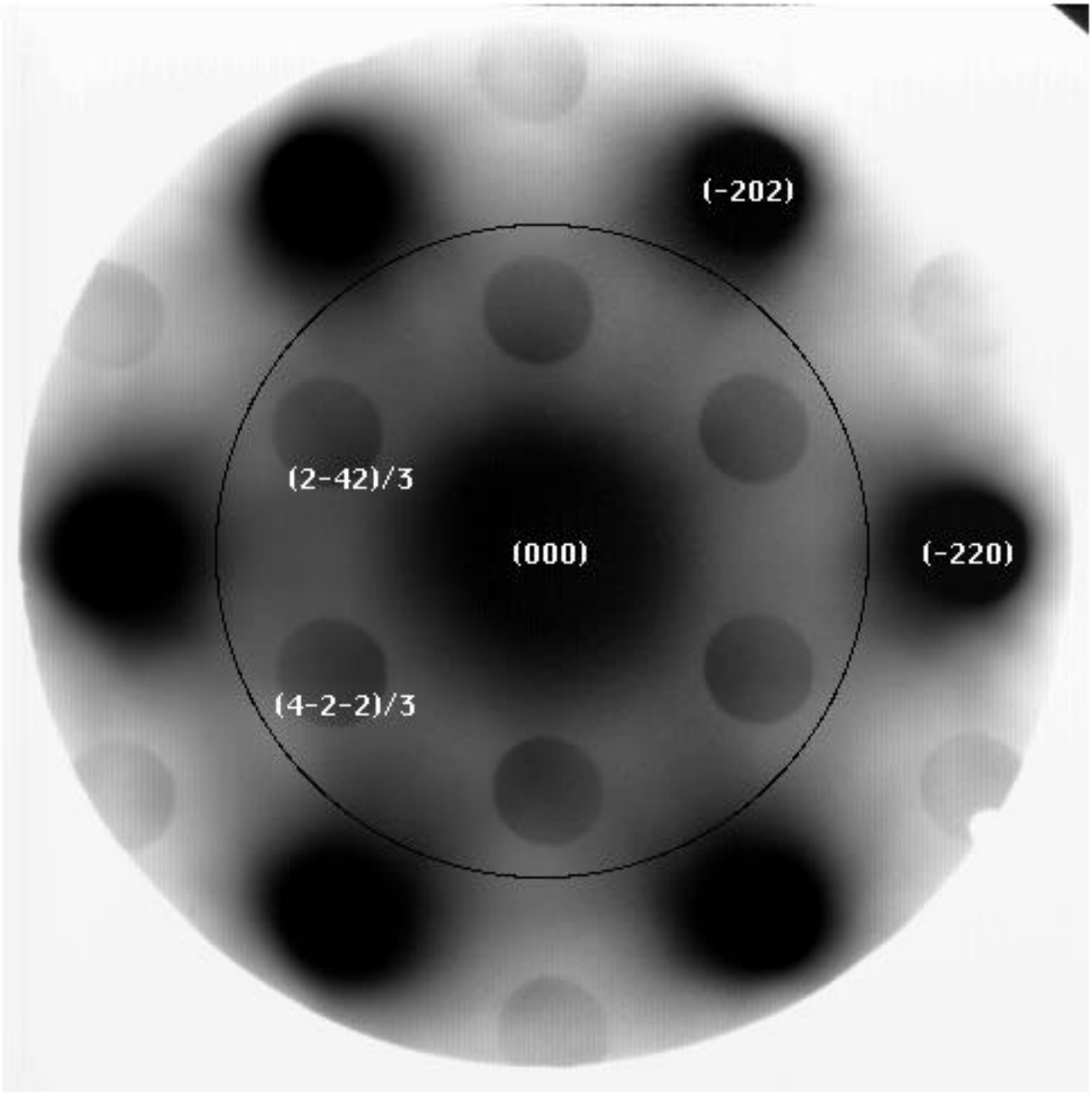

Figure 1. Experimental CBED pattern from an intrinsic stacking fault on (111) in silicon lying normal to the beam. The "termination" {-422}/3 type forbidden reflections can be clearly seen inside the bulk allowed {220} reflections. Circle shows aperture used for imaging (Philips FEG 400 ST, 120 kV. Probe size about 2 nm.). The (1-11) reciprocal lattice point lies directly above (2,-4,2)/3.

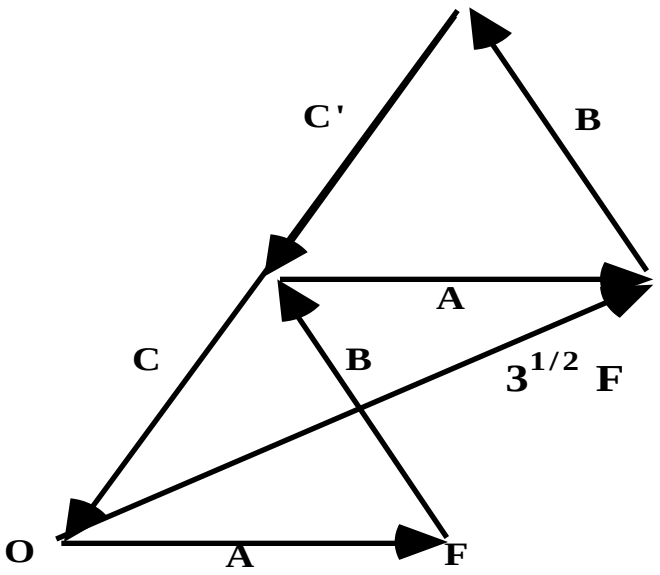

Figure 2. Argand diagram for a {-422}/3 reflection in silicon. Real part of structure factor F plotted vertically, imaginary part horizontal. The kinematic amplitude of Bragg scattering is proportional to a vector from the origin to one corner of the figure. A crystal with stacking sequence ABCAB/ABCA produces the amplitude √3 F shown.

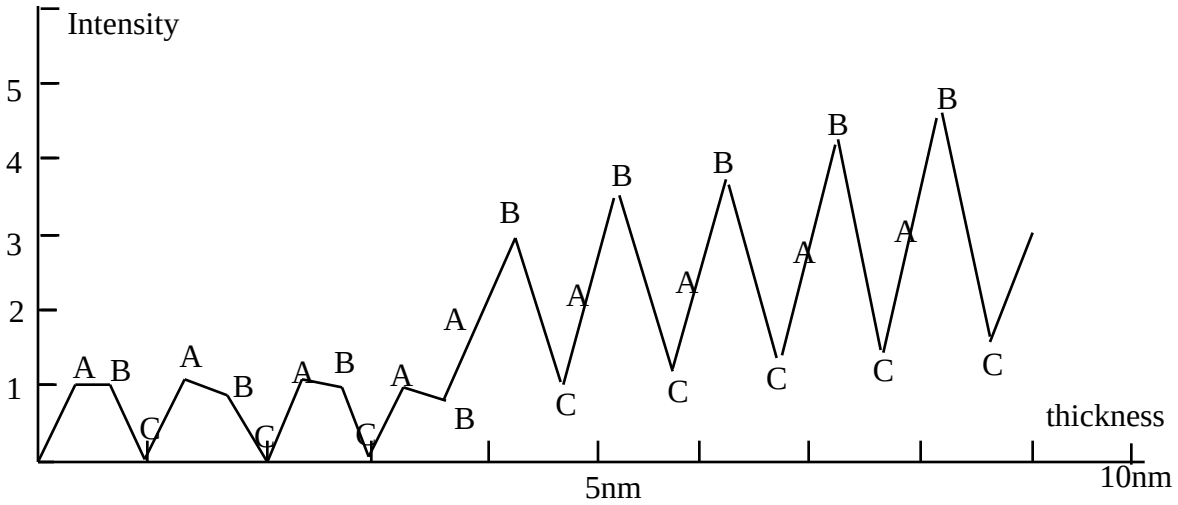

Figure 3. Multiple scattering calculations (using 1000 beams) giving the thickness dependance of the termination reflection (-2-24)/3 in silicon at 100 kV, with beam along [111]. Each letter represents the addition of one atomic layer. A stacking fault occurs at ABA. Three of the six beams are equivalent.

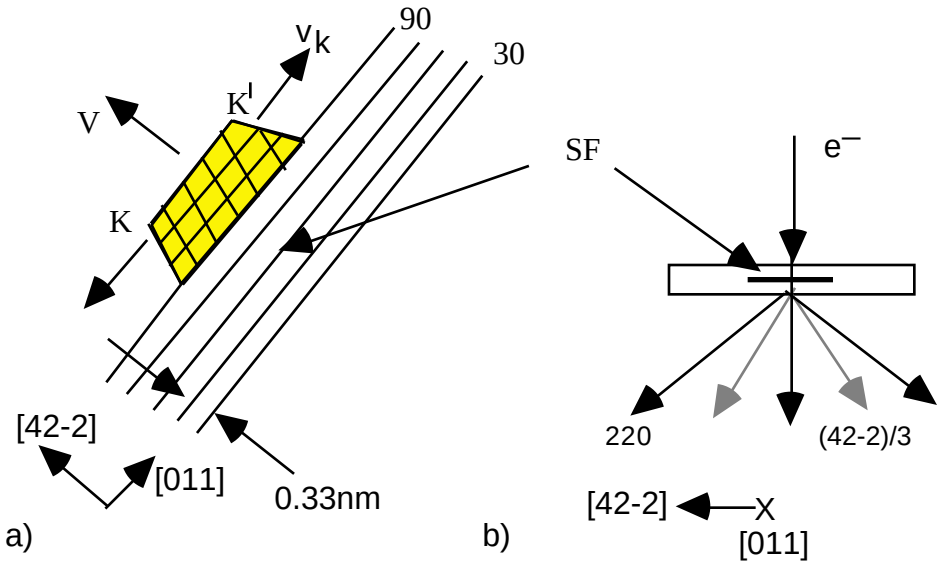

Figure 4.(a). Stacking fault SF on (111) plane (parallel to page) separating 30^o and 90^o partial dislocation lines, with low-energy Peierls valleys along [110] and kink pair K, K' shown. By running together these kinks advance the dislocation line in direction V. (b) shows side view, along [011], indicating "forbidden" (42-2)/3 Bragg reflections generated by SF, and bulk (220) beams.

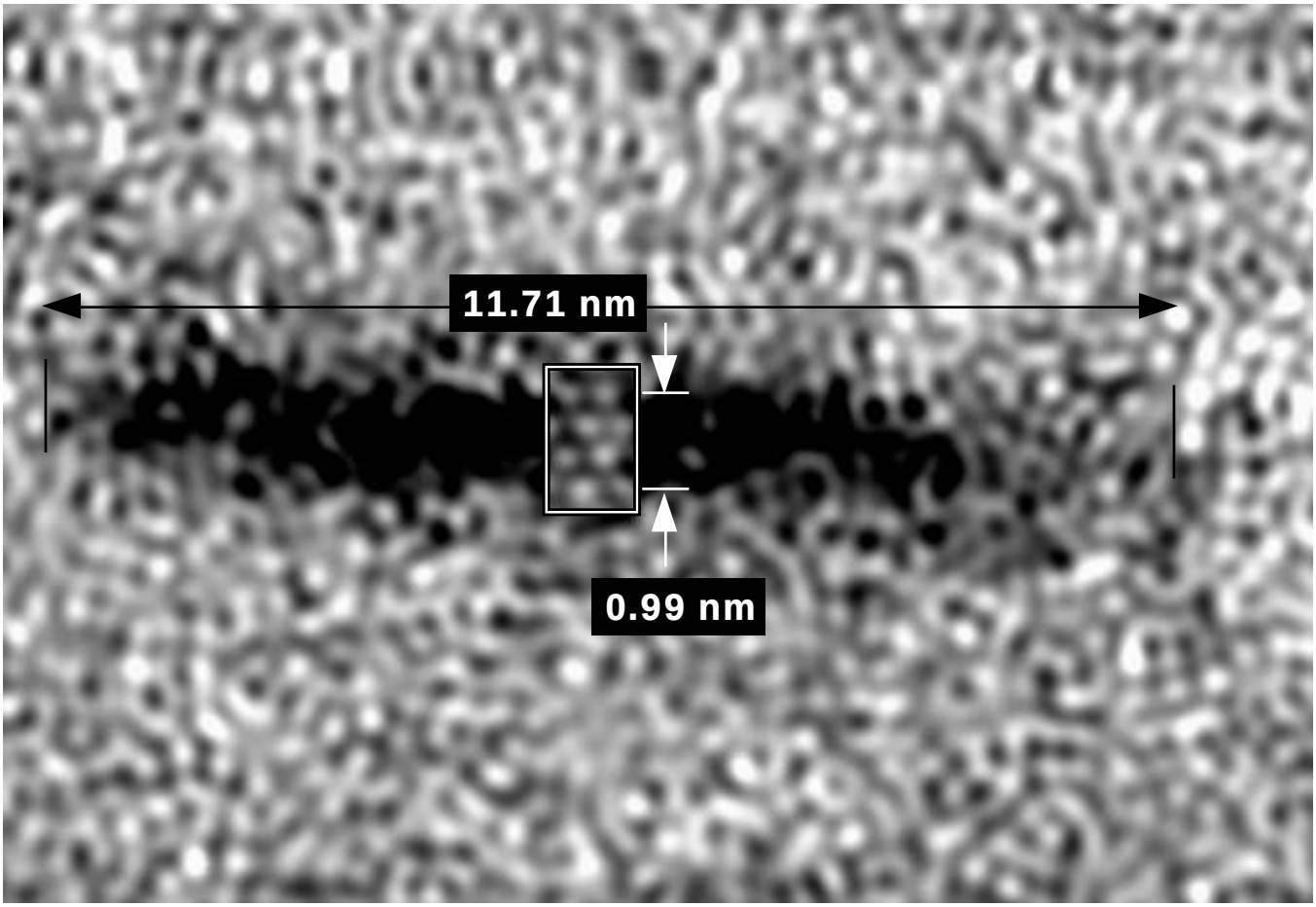

Figure 5(a). Difference between filtered video images of a moving 90^{o} partial dislocation in silicon at 600^{o}C, viewed along [111]. Dark strip is SF three Peierls valleys wide (0.99nm), eliminated by passage of several kinks. Inset shows experimental SF image for scale. The dark patch is a portion of the shaded region in figure 4(a).

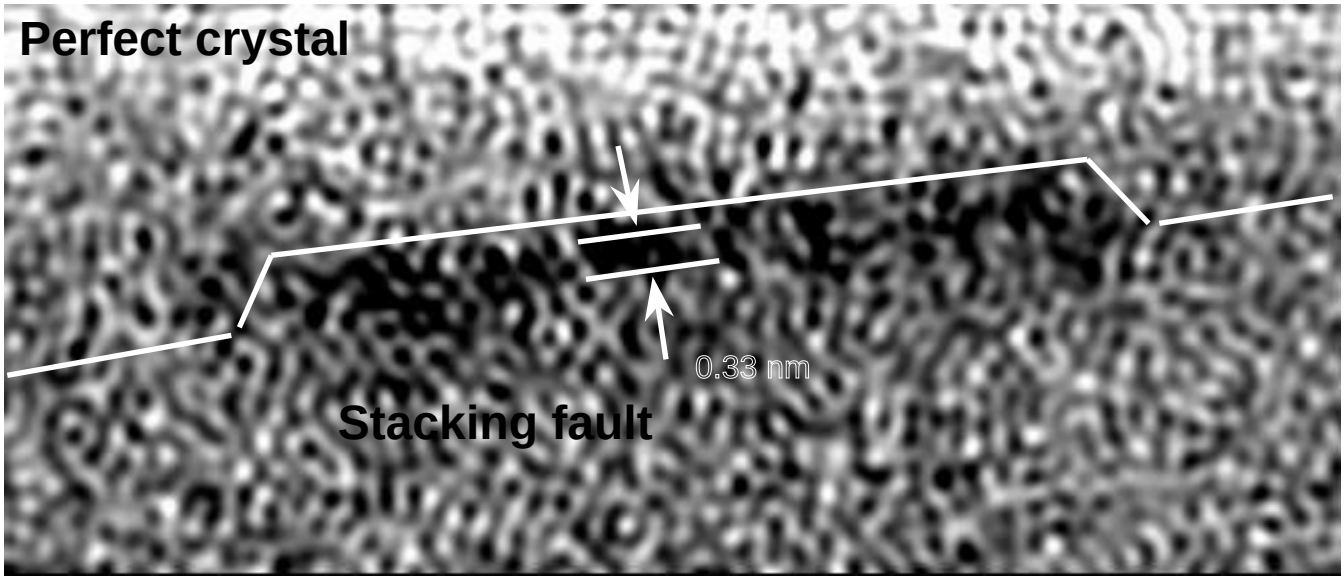

Figure 5(b). Similar for 90^{o} partial segment , one Peierls valley wide.

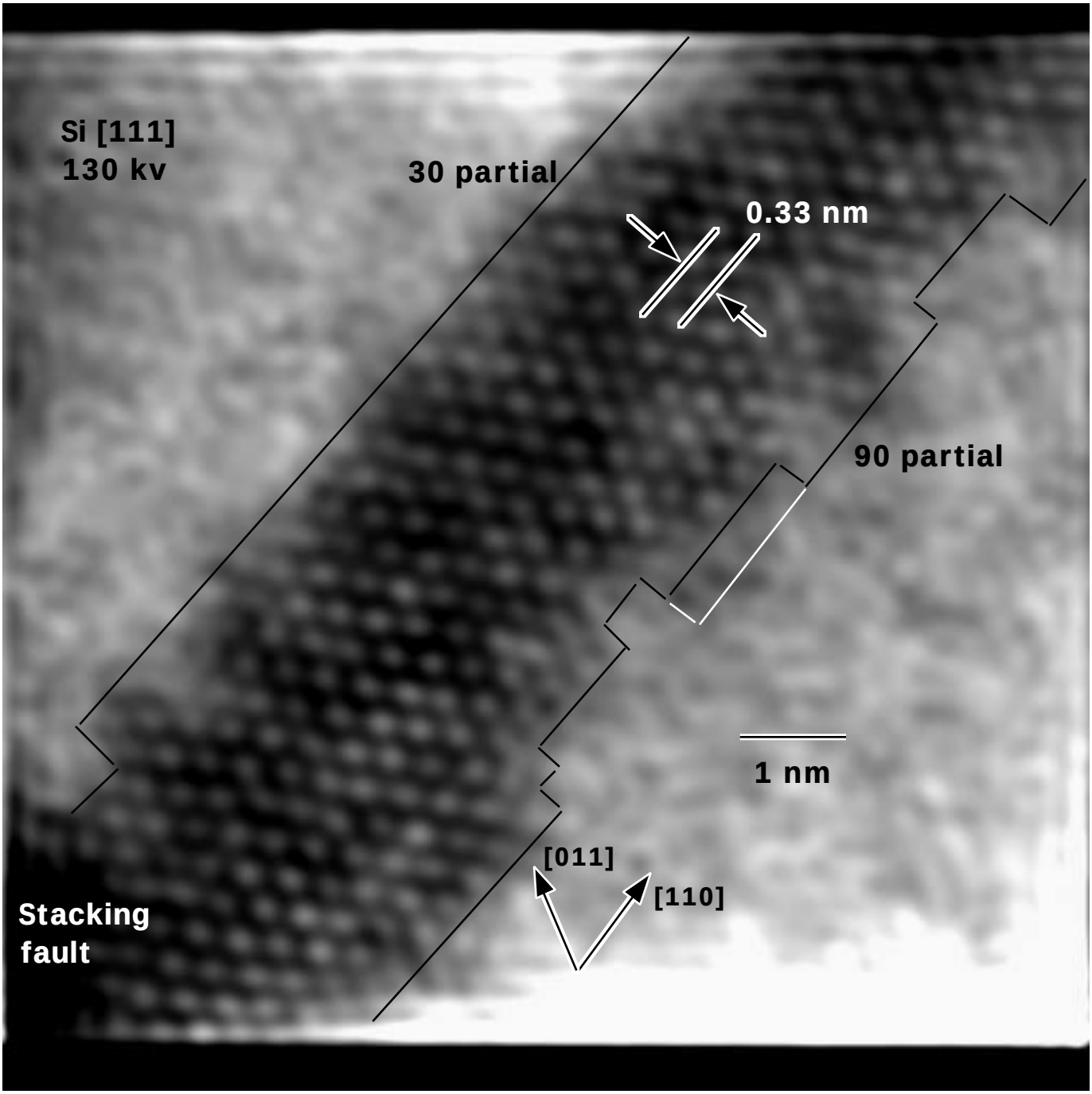

Figure 6. TEM image of dissociated 60^{o} dislocation in silicon after relaxation. The bright diagonal band of regular dots are six-membered rings in the ribbon of SF separating 30^{o} and 90^{o} partial dislocation lines. Black lines run along cores of the two partial dislocations. Fine white line shows typical alternative boundary used to estimate error in counting kinks.

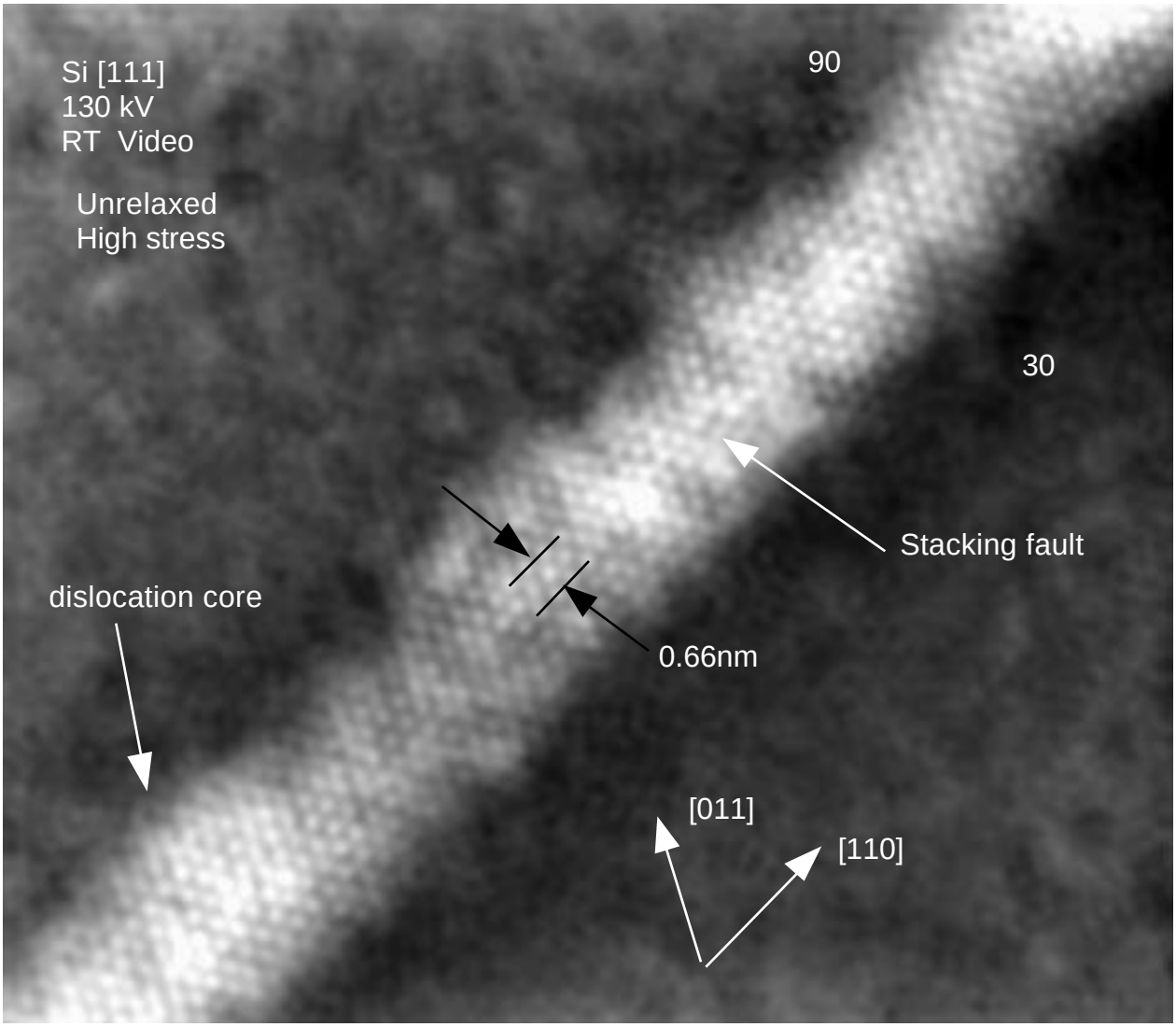

Figure 7. Similar to figure 6, but for an unrelaxed pair of partials spaced more closely than the equilibrium separation.